Journal Title
XX(X):2–33

DOI: 10.1177/ToBeAssigned
www.sagepub.com/

Micromechanics based discrete damage model with multiple non-smooth yield surfaces: theoretical formulation, numerical implementation and engineering applications

Wencheng Jin[1] and Chloé Arson[1]

Abstract

The discrete damage model presented in this paper accounts for 42 non-interacting crack microplanes directions. At the scale of the Representative Volume Element (RVE), the free enthalpy is the sum of the elastic energy stored in the non-damaged bulk material and in the displacement jumps at crack faces. Closed cracks propagate in pure mode II, whereas open cracks propagate in mixed mode (I/II). The elastic domain is at the intersection of the yield surfaces of the activated crack families, and thus describes a non-smooth surface. In order to solve for the 42 crack densities, a Closest Point Projection algorithm is adopted locally. The RVE inelastic strain is calculated iteratively, by using Newton-Raphson method. The proposed damage model was rigorously calibrated for both compressive and tensile stress paths. FEM simulations of triaxial compression tests showed that the transition between brittle and ductile behavior at increasing confining pressure can be captured. The cracks' density, orientation and location predicted in the simulations are in agreement with experimental observations made during compression and tension tests, and accurately show the difference between tensile and compressive strength. Plane stress tension tests simulated for a fiber-reinforced brittle material also demonstrated that the model can be used to interpret crack patterns, design composite structures and recommend reparation techniques for structural elements subjected to multiple damage mechanisms.

Keywords
Brittle/ductile transition, Continuum Damage Mechanics, Microplanes, Homogenization, Multiple yield surfaces, Closest Point Projection algorithm, FEM

Introduction

Brittle materials such as concrete, rock, and ceramic composites, exhibit a complex mechanical behavior at the macro-scale, including stress-induced damage and stiffness anisotropy, non-linear stress/strain relationships and volumetric dilation, unilateral effects due to crack closure, and a transition from brittle to ductile behavior at increasing confining stress (Krajcinovic et al. 1991; Chiarelli et al. 2003). All of these effects can be explained by the nucleation and propagation of micro-cracks at the grain boundaries and/or from pore spaces. Three approaches were adopted so far to model these microstructural effects on the behavior of the Representative Volume Element (RVE) (Yuan and Harrison 2006): Continuum Damage Mechanics (CDM), statistical formulations and micromechanics.

CDM is based on the thermodynamics of irreversible processes (Chaboche 1981; Simo and Ju 1987; Chaboche 1988; Krajcinovic 1989; Collins and Houlsby 1997). Damage tensors are used as internal state variables and incorporated into the expression of the RVE free energy in order to account for stress-induced anisotropy. Damage tensors are similar to crack density tensors in micromechanics or fabric tensors in structural geology, and are usually of order two (Murakami 1988; Mazars and Pijaudier-Cabot 1989; Halm and Dragon 1996) or of order four (Simo and Ju 1987; Ju 1989). CDM models are phenomenological in nature, which implies that damage tensors essentially measure the damaged mechanical effects rather than the microstructure evolution itself (Swoboda and Yang 1999a). As a result, damage evolution laws are arbitrarily crafted to match a macroscopic behavior (usually represented by stress/strain curves), and do not represent any clear physical mechanism. The behavior of brittle geomaterials depends on the sign of the applied stress/strain. Therefore, the damage driving force (i.e. the energy release rate that is work-conjugate to damage) has to be split into positive and negative components, which are introduced in two different damage criteria (one for tension, one for compression) (Lubarda et al. 1994; Frémond and Nedjar 1996; Comi and Perego 2001). The singularities of the damage surfaces raise convergence issues in Finite Element Methods (FEM). Unilateral effects, induced by crack closure with partial recovery of compression strength, require additional material parameters and adds even more complexity to the FEM implementation of CDM models Chaboche (1992, 1993); Halm and Dragon (1996).

[1]School of Civil and Environmental Engineering, Georgia Institute of Technology, USA

Corresponding author:
Chloé Arson, Georgia Institute of Technology, 790 Atlantic Dr., Atlanta, GA , USA.
Email: chloe.arson@ce.gatech.edu

Statistical formulations are based on microstructure descriptors, such as grain/pore size/orientation/shape. The RVE is seen as a statistical distribution of solids endowed with different local stiffness and strength parameters (Weibull 1951). Stress concentrations are calculated around heterogenities, local failure criteria are checked, and local field variables are updated. The RVE response is modeled by statistical averaging methods. In continuum mechanics approaches such as FEMs, local mechanical properties are assigned to Finite Elements that are distributed in space according to microstructure statistical descriptors (Amitrano et al. 1999; Tang et al. 2000; Fang and Harrison 2002). In discrete approaches, the RVE is represented by rigid or elastic spheres or irregularly shaped elements, which interact according to constitutive laws that depend on the statistical properties (Blair and Cook 1998; Amitrano et al. 1999; Jing 2003; Potyondy and Cundall 2004). Statistical approaches allow simulating micro crack initiation, growth and coalescence into macro fractures. However, statistical micro crack properties have to be determined by trial and error to fit the macro material behavior, which is somewhat random and time-consuming.

In micromechanical models, the RVE behavior is obtained by homogenization, after calculating local stresses and displacements at crack faces. In the dilute homogenization scheme such as Taylor's model (e.g. Krajcinovic and Fanella (1986); Gambarotta and Lagomarsino (1993); Pensée et al. (2002); Pensee and Kondo (2003); Swoboda and Yang (1999a); Espinosa (1995); Feng and Yu (2010)), cracks are assumed to evolve independently from each other, and the RVE behavior is obtained by superposition. By contrast, crack interaction is accounted for in the self-consistent method (e.g., (Budiansky and O'connell 1976; Lee and Ju 1991; Ju and Lee 1991)) and the Mori-Tanaka scheme (e.g., Mori and Tanaka (1973); Zhu et al. (2008, 2009)). Microscopic interactions were also accounted for by multiplying deformation gradients induced by various sets of defects (e.g., (Clayton 2010)). Homogenization schemes were compared in several studies, including Krajcinovic and Sumarac (1989); Ju (1991). Simulation results indicate that the dilute scheme is accurate prior to the peak strength. Micro-crack evolution laws are either derived from fracture mechanics (e.g., Kachanov (1982a); Krajcinovic and Fanella (1986); Ju and Lee (1991); Yu and Feng (1995)) or damage growth criteria (e.g., (Swoboda and Yang 1999b,a; Pensée et al. 2002; Pensee and Kondo 2003)). In the former case, stress intensity factors accounting or not for crack interactions are computed for Mode I splitting, Mode II frictional sliding or mixed Mode propagation. In order to predict crack kinking (i.e., wing crack formation), it is often assumed that a secondary crack aligned with the maximum compressive stress initiates and grows due to stress- or displacement- driven energy release rates (e.g. Kachanov (1982b); Horii and Nemat-Nasser (1986); Lee and Ju (1991); Lehner and Kachanov (1996)). The advantage of fracture mechanics is that a direct link is established between micro-crack propagation and macroscopic mechanical behavior, and the material parameters involved all have a clear physical meaning. However, the assumptions required to describe the crack arrangement and to predict the kinking direction limit fracture mechanics - based approaches to a few loading paths only. In the latter case, self-similar propagation laws are formulated in terms of force that is work-conjugated to damage (or crack density). One of the major challenges raised by damage growth criteria is numerical

implementation into FEM codes, which requires sophisticated algorithms and important computational resources.

The main objective of the present paper is to formulate a damage model based on a discrete description of damage microplanes, and to implement it in a FEM code in order to capture inelastic deformation, unilateral effects and distinct strength and stiffness properties in tension and compression, for complex stress paths involving the propagation of both open and closed cracks in mode I, mode II, and mixed mode. First, the theoretical formulation of the discrete damage model, based on Bazant's 2×21 integration method and the dilute homogenization scheme, is presented. Different yield criteria are employed for open and closed cracks for each microplane orientation considered in the integration scheme. The elastic domain of the RVE is defined by the intersection of activated damage surfaces, and the RVE inelastic strain tensor is obtained by superposing the irreversible strains induced by all the activated crack openning displacements. Damage yield surfaces are not smooth, which requires a special treatment to allow numerical implementation. Then, we present a local Closest Point Projection algorithm, which we use to determine the set of activated cracks and the corresponding increments of crack density. We explain the detailed calculations required to calculate the Jacobian matrix at the material point, which is needed in the Newton-Raphson method used to solve the non linear FEM equations. We also validate the implementation of the resolution algorithm by comparing material-point simulation results to those obtained with a one-element FEM model. In the final section of the paper, we calibrate the proposed discrete damage model against experimental results of triaxial compression and uniaxial tension tests reported in the literature. We simulate triaxial compression tests and Hassanzadeh's direct tension test with the calibrated model parameters obtained for concrete. We also model a composite made of a brittle matrix reinforced by stiff elastic fibers to study the influence of reinforcement orientations on the formation of crack patterns.

Theoretical formulation of the discrete damage model

Micromechanics-based free enthalpy

We formulate a new damage model in which the expression of the free enthalpy is obtained from micromechanics principles. In the following, we consider a RVE of volume Ω_r and external boundary $\partial\Omega_r$, in which a large number of penny shaped microscopic cracks of various orientations are embedded in an isotropic linear elastic matrix of compliance tensor $\mathbb{S}^m$. Each microscopic crack is characterized by its normal direction $\overrightarrow{n}$ and its radius a, which is at least 100 times smaller than the RVE size. Opposite crack faces are noted ω^+ and ω^-, with normal vectors $\overrightarrow{n}^+$ and $\overrightarrow{n}^-$ respectively. The displacement jump is noted:

$$[\overrightarrow{u}] = \overrightarrow{u}^+ - \overrightarrow{u}^- \tag{1}$$

Where $\overrightarrow{u}^+$ (respectively $\overrightarrow{u}^-$) denotes the displacement vector at face ω^+ (respectively ω^-). We consider a uniform stress field $\boldsymbol{\sigma}$ applied at the boundary $\partial\Omega_r$. The displacement field at the RVE scale is calculated by superposition, by adding up the displacement field

in the elastic matrix in the absence of cracks and the displacement field induced by the opening and sliding of micro-crack faces (Fig.1).

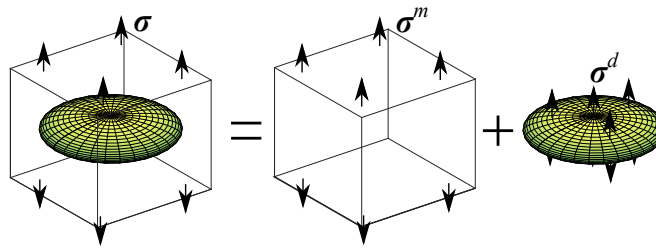

Figure 1. Homogenization based on the principle of superposition

We consider that the mechanical interaction between cracks is negligible and we use a dilute homogenization scheme to calculate the crack displacement jumps. As a result, the average micro stress is equal to the stress applied to the RVE, and we have:

$$\boldsymbol{\sigma} = \frac{1}{\Omega_r}\int_{\Omega_r}[\boldsymbol{\sigma}^m(x) + \boldsymbol{\sigma}^d(x)]\mathrm{d}x \tag{2}$$

In which $\boldsymbol{\sigma}^d$ is the stress field that is applied at micro-crack faces and $\boldsymbol{\sigma}^m$ is the stress field in the linear elastic matrix. Moreover, the static constraint imposed by the dilute homogenization scheme is applied to the elastic cracked RVE when crack do not propagate, which implies that the local stress $\boldsymbol{\sigma}^d$ is the direct projection of the macro stress $\boldsymbol{\sigma}$ on crack faces. Consequently, for each crack, the local stress that applies at the crack faces is self-equilibrating and the matrix stress is equal to the macro stress:

$$0 = \int_{\omega}\boldsymbol{\sigma}^d(x)\mathrm{d}x, \quad \boldsymbol{\sigma} = \boldsymbol{\sigma}^m \tag{3}$$

The elastic strain tensor of the matrix $\boldsymbol{\epsilon}^e$ depends on the undamaged compliance tensor $\mathbb{S}^m$, as follows:

$$\boldsymbol{\epsilon}^e = \mathbb{S}^m : \boldsymbol{\sigma}^m = \mathbb{S}^m : \boldsymbol{\sigma}. \tag{4}$$

In the dilute homogenization scheme adopted here, we treat each micro-crack as a single crack embedded in an infinite elastic homogeneous matrix, which allows calculating the displacement jumps from fracture mechanics principles (Horii and Nemat-Nasser 1983; Kachanov et al. 2013). Considering a penny shaped crack of radius a subjected to a uniformly distributed normal stress p (respectively shear stress $\overrightarrow{\tau}$) at its faces and embedded in an infinite elastic medium with Young's modulus E_0 and Poisson's ratio ν_0, the average normal (respectively shear) displacement jump, also

known as Crack Opening Displacement (COD), is expressed as:

$$\begin{aligned}\langle[u_n]\rangle &= \frac{16}{3}\frac{1-\nu_0^2}{\pi E_0}pa \\ \langle[\overrightarrow{u_t}]\rangle &= \frac{32}{3}\frac{1-\nu_0^2}{(2-\nu_0)\pi E_0}\overrightarrow{\tau}a\end{aligned} \tag{5}$$

We consider that the RVE contains families of penny shaped cracks that have same orientation $\overrightarrow{n_i}$ and same radius a_i. Such a family of micro-cracks is shown in Fig.2(a). If the family contains N cracks, the volume fraction of the normal and shear displacement jumps can be calculated as follows:

$$\begin{aligned}\beta_i &= \frac{N}{\Omega_r}\langle[u_n]\rangle\pi a_i^2 = \rho_i c_0 \boldsymbol{\sigma}^d : (\overrightarrow{n_i}\otimes\overrightarrow{n_i}) = \rho_i c_0 \boldsymbol{\sigma} : (\overrightarrow{n_i}\otimes\overrightarrow{n_i}) \\ \overrightarrow{\gamma_i} &= \frac{N}{\Omega_r}\langle[\overrightarrow{u_t}]\rangle\pi a_i^2 = \rho_i c_1[\boldsymbol{\sigma}^d\cdot\overrightarrow{n_i} - (\overrightarrow{n_i}\cdot\boldsymbol{\sigma}^d\cdot\overrightarrow{n_i})\overrightarrow{n_i}] = \rho_i c_1[\boldsymbol{\sigma}\cdot\overrightarrow{n_i} - (\overrightarrow{n_i}\cdot\boldsymbol{\sigma}\cdot\overrightarrow{n_i})\overrightarrow{n_i}]\end{aligned} \tag{6}$$

Where $\overrightarrow{\tau} = \boldsymbol{\sigma}\cdot\overrightarrow{n_i} - (\overrightarrow{n_i}\cdot\boldsymbol{\sigma}\cdot\overrightarrow{n_i})\overrightarrow{n_i}$. Note that according to the dilute scheme assumption, the direct projection of the macro stress $\boldsymbol{\sigma}$ on crack faces is equal to the direct projection of the local stress $\boldsymbol{\sigma}^d$ on crack faces. $\rho_i = Na_i^3/\Omega_r$ is the crack density parameter along the direction $\overrightarrow{n_i}$ introduced in (Budiansky and O'connell 1976) . Note that the value of ρ_i can exceed one. The coefficient c_0 (respectively c_1) is defined as the normal (respectively shear) elastic compliance of the crack (Budiansky and O'connell 1976; Kachanov 1992):

$$c_0 = \frac{16}{3}\frac{1-\nu_0^2}{E_0}, \quad c_1 = \frac{32}{3}\frac{1-\nu_0^2}{(2-\nu_0)E_0} \tag{7}$$

A normal displacement jump can only be induced by a tensile force, i.e. for $\overrightarrow{n_i}\cdot\boldsymbol{\sigma}\cdot\overrightarrow{n_i} \leq 0$ (in which compression is counted positive, according to the soil mechanics convention). The unilateral contact condition at crack faces can be expressed as

$$[u_n] \geq 0, \quad \sigma_{nn} = \overrightarrow{n}\cdot\boldsymbol{\sigma}\cdot\overrightarrow{n} \leq 0, \quad [u_n]\sigma_{nn} = 0 \tag{8}$$

The average strain due to the displacement jumps of the all the micro-cracks of the family with normal $\overrightarrow{n_i}$ is calculated as:

$$\begin{aligned}\boldsymbol{\epsilon}^d &= \frac{N}{\Omega_r}\int_{\partial\omega^+}[u_n](\overrightarrow{n_i}\otimes\overrightarrow{n_i})\mathrm{d}S + \frac{N}{2\Omega_r}\int_{\partial\omega^+}([\overrightarrow{u_t}]\otimes\overrightarrow{n_i} + \overrightarrow{n_i}\otimes[\overrightarrow{u_t}])\mathrm{d}S \\ &= \beta_i\overrightarrow{n_i}\otimes\overrightarrow{n_i} + \frac{1}{2}(\overrightarrow{\gamma_i}\otimes\overrightarrow{n_i} + \overrightarrow{n_i}\otimes\overrightarrow{\gamma_i})\end{aligned} \tag{9}$$

According to the principle of superposition, the Helmholtz free energy W^* of the RVE containing the N cracks of orientation $\overrightarrow{n_i}$ is the sum of the elastic deformation energy of

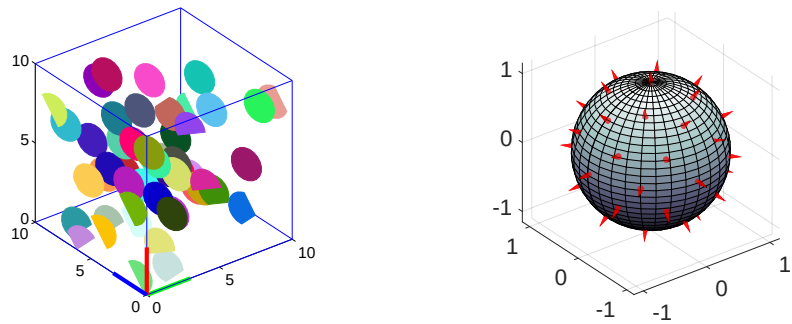

(a) Single crack family (b) Discrete crack family orientations

Figure 2. (a)Sketch of a RVE with one family of parallel equally sized penny shaped micro-cracks; (b) Repartition of the integration points on the unit sphere, following the microplane approach based on 2×21 points presented in (Bažant and Oh 1986)

the matrix and the energy stored in the micro cracks displacement jumps, as follows:

$$W^* = \frac{1}{2}\boldsymbol{\epsilon}^e : \mathbb{C}^m : \boldsymbol{\epsilon}^e + \frac{1}{2}\boldsymbol{\sigma} : [\beta_i \overrightarrow{n_i} \otimes \overrightarrow{n_i} + \frac{1}{2}(\overrightarrow{\gamma_i} \otimes \overrightarrow{n_i} + \overrightarrow{n_i} \otimes \overrightarrow{\gamma_i})] \tag{10}$$

In which it is recalled that $\sigma : \overrightarrow{n_i} \otimes \overrightarrow{n_i} = \sigma^d : \overrightarrow{n_i} \otimes \overrightarrow{n_i}, \sigma : \overrightarrow{n_i} \otimes \overrightarrow{\gamma_i} = \sigma^d : \overrightarrow{n_i} \otimes \overrightarrow{\gamma_i}$. The Gibbs energy (free enthalpy) is obtained by Legendre transformation, as follows:

$$G^* = \boldsymbol{\sigma} : \boldsymbol{\epsilon}^E - W^* \tag{11}$$

In which $\boldsymbol{\epsilon}^E = \boldsymbol{\epsilon}^e + \boldsymbol{\epsilon}^d$ is the RVE elastic strain. As a result, G^* is expressed as:

$$\begin{aligned} G^* &= \frac{1}{2}\boldsymbol{\sigma} : \mathbb{S}^m : \boldsymbol{\sigma} + \frac{1}{2}\boldsymbol{\sigma} : \boldsymbol{\epsilon}^d \\ &= \frac{1}{2}\boldsymbol{\sigma} : \mathbb{S}^m : \boldsymbol{\sigma} + \frac{1}{2}\boldsymbol{\sigma} : [\beta_i \overrightarrow{n_i} \otimes \overrightarrow{n_i} + \frac{1}{2}(\overrightarrow{\gamma_i} \otimes \overrightarrow{n_i} + \overrightarrow{n_i} \otimes \overrightarrow{\gamma_i})] \end{aligned} \tag{12}$$

By substituting Eq.6 into the expression of the free enthalpy above, and introducing the unilateral contact condition in Eq.8, we get:

$$G^* = \frac{1}{2}\boldsymbol{\sigma} : \mathbb{S}^m : \boldsymbol{\sigma} + \frac{1}{2}c_0\rho_i H(\overrightarrow{n_i} \cdot \boldsymbol{\sigma} \cdot \overrightarrow{n_i})\boldsymbol{\sigma} : \mathbb{N}_i : \boldsymbol{\sigma} + \frac{1}{2}c_1\rho_i\boldsymbol{\sigma} : \mathbb{T}_i : \boldsymbol{\sigma} \tag{13}$$

Where $H(\cdot)$ is the Heaviside jump function and $\overrightarrow{n_i} \cdot \boldsymbol{\sigma} \cdot \overrightarrow{n_i} = \sigma^i_{nn}$ is the normal stress at the crack face. The fourth order normal (respectively, tangent) operator $\mathbb{N}_\alpha$ (respectively, $\mathbb{T}_\alpha$) is defined by:

$$\begin{aligned} \mathbb{N}_\alpha &= N^\alpha_{ijkl} = n^\alpha_i n^\alpha_j n^\alpha_k n^\alpha_l \\ \mathbb{T}_\alpha &= T^\alpha_{ijkl} = \frac{1}{4}(n^\alpha_i n^\alpha_k \delta_{jl} + n^\alpha_i n^\alpha_l \delta_{jk} + \delta_{ik} n^\alpha_j n^\alpha_l + \delta_{il} n^\alpha_j n^\alpha_k) - n^\alpha_i n^\alpha_j n^\alpha_k n^\alpha_l \end{aligned} \tag{14}$$

In which n_j^{α} is the unit normal vector of each direction α. We can calculate the total Gibbs energy of the RVE by integrating G^* for a distribution of crack orientations $\rho(n)$, over the unit sphere $S^2 = \{\overrightarrow{n}, |\overrightarrow{n}| = 1\}$, as follows:

$$G = \frac{1}{2}\boldsymbol{\sigma} : \mathbb{S}^m : \boldsymbol{\sigma} + \frac{1}{8\pi}\int_{S^2} \rho(\overrightarrow{n})\{c_0\, H(\sigma_{nn}^i)\boldsymbol{\sigma} : \mathbb{N}_i : \boldsymbol{\sigma} + c_1\, \boldsymbol{\sigma} : \mathbb{T}_i : \boldsymbol{\sigma}\}\mathrm{d}S \tag{15}$$

Since the calculation of the integral above is impractical for a continuous distribution $\rho(\overrightarrow{n})$, we use a numerical integration scheme, with M integration points:

$$G = \frac{1}{2}\boldsymbol{\sigma} : \mathbb{S}^m : \boldsymbol{\sigma} + \frac{1}{2}\sum_{i=1}^{M} w_i \rho_i \Big[\boldsymbol{\sigma} : (c_0\, H(\sigma_{nn}^i)\mathbb{N}_i + c_1\, \mathbb{T}_i) : \boldsymbol{\sigma}\Big] \tag{16}$$

Where w_i is the weight in direction n_i. We adopt Bazant's discrete scheme with 2×21 microplanes (Bažant and Oh 1986) as shown in Fig.2(b). Note that the calculation of G requires M calculations at each time step. Increasing M can increase exponentially the computational cost of the numerical integration. Bazant's 2×21 scheme provides satisfactory accuracy at reasonable computation cost. For a detailed discussion about the performance of the numerical integration scheme, the reader is referred to (Ehret et al. 2010; Levasseur et al. 2013).

Thermodynamically consistent yield function and evolution law

The derived Gibbs energy in Eq.16 only accounts for the elastic crack displacement jump, without considering crack growth. Moreover, triaxial compression tests on brittle materials, such as rock and concrete, show that irreversible deformation exists after unloading, which indicates that inelastic deformation is an additional dissipation mechanism that is coupled to micro-crack propagation. In order to account for irreversible crack debonding (i.e. crack radius growth) accompanied by inelastic deformation, we introduce the inelastic strain $\boldsymbol{\epsilon}^{in}$ in the formulation. A hyper-elastic framework (Collins and Houlsby 1997), in which the RVE strain tensor $\boldsymbol{\epsilon}$ is split into a pure elastic part $\boldsymbol{\epsilon}^e$ which corresponds to the deformation of elastic matrix, an additional elastic part $\boldsymbol{\epsilon}^d$ which represents the micro-crack elastic strain, and the inelastic deformation $\boldsymbol{\epsilon}^{in}$, is adopted as follows:

$$\boldsymbol{\epsilon} = \boldsymbol{\epsilon}^e + \boldsymbol{\epsilon}^d + \boldsymbol{\epsilon}^{in} = \boldsymbol{\epsilon}^E + \boldsymbol{\epsilon}^{in} \tag{17}$$

In which:

$$\begin{aligned}
\boldsymbol{\epsilon}^E &= \boldsymbol{\epsilon}^e + \boldsymbol{\epsilon}^d = \frac{\partial G}{\partial \boldsymbol{\sigma}} \\
\boldsymbol{\epsilon}^e &= \frac{1+\nu_0}{E_0}\boldsymbol{\sigma} - \frac{\nu_0}{E_0}\mathrm{Tr}(\boldsymbol{\sigma})\boldsymbol{\delta} \\
\boldsymbol{\epsilon}^d &= \sum_{i=1}^{M} \rho_i w_i (c_0 \mathbb{N}_i H(\sigma_{nn}^i) + c_1 \mathbb{T}_i) : \boldsymbol{\sigma}
\end{aligned} \tag{18}$$

For each micro-plane orientation i, conjugation relationships are established to calculate the damage driving force Y_i:

$$Y_i = \frac{\partial G}{\partial \rho_i} = \frac{1}{2} w_i \boldsymbol{\sigma} : (c_0 \mathbb{N}_i H(\sigma^i_{nn}) + c_1 \mathbb{T}_i) : \boldsymbol{\sigma} \tag{19}$$

In the framework of thermodynamics, the damage driving force in direction i is defined as the energy release rate necessary to propagate a unit crack density in that direction. Additionally, in fracture mechanics, the energy release rate must exceed the crack resistance $R(\rho_i)$ to allow the crack boundary to grow. Thus, the most general expression for the yield surface is:

$$f_i(\rho_i, Y_i) = Y_i - R(\rho_i) \tag{20}$$

Where $R(\rho_i)$ is the equation of the crack resistance curve, which accounts for the heterogeneities inside the material matrix and depends on the crack radius (crack density). According to Eq.19, the expression of the energy release rate is quadratic in deviatoric stress when the unilateral contact condition is not satisfied. However, rock samples subjected to compression tests exhibit a brittle behavior at low confining pressure and a ductile behavior at higher confining pressure. In order to capture this brittle-ductile transition, a term depending on the mean stress is added to Eq.20. The yield criterion adopted in the proposed model is inspired from Drucker-Prager model, and is expressed as follows:

$$f_i(\rho_i, Y_i) = Y_i - \alpha \mathrm{Tr}\boldsymbol{\sigma} - R(\rho_i) \tag{21}$$

From a mechanical point of view, the expression of the resistance curve $R(\rho_i)$ controls the hardening or softening behavior after the initial yield surface is reached. In this study, we consider that $R(\rho_i)$ is a linear function of the crack density ρ_i (Pensee and Kondo 2003) and we emphasize that our model is only applicable for dilute distributions of micro-cracks, i.e. before crack coalescence and before the peak of strength. In addition, we distinguish the increase of open crack density in Modes I & II (when the unilateral condition is satisfied for the i^{th} microplane direction) and the increase of closed crack density in Mode II (when the unilateral condition is not satisfied for the i^{th} microplane direction), as follows:

$$f_i(\rho_i, Y_i) = Y_i - \alpha \mathrm{Tr}\boldsymbol{\sigma} - k(1 + \eta\rho_i) \tag{22}$$

Where $k = k_c, \eta = \eta_c$ if cracks of the i^{th} family are closed , and $k = k_o, \eta = \eta_o$ if cracks of the i^{th} family are open. Each crack yield criterion f_i is associated with one particular crack family. The macroscopic yield surface is the boundary of the elastic domain intersected by all the activated crack yield surfaces, as shown in Fig.3. For each active microplane direction, the closed crack criterion is activated if the macroscopic stress projected on the crack plane is a compression, and the open crack criterion is activated if the macroscopic stress projected on the crack plane is a tension. Note that in Eq. 22, the crack yield criterion f_i can be rewritten in the form of a function of stress and crack density only, because the energy release rate is a function of stress. As a result, the

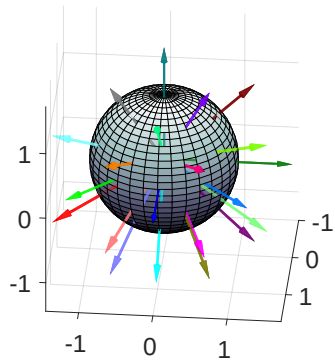

(a) Color code used for microplane orientations

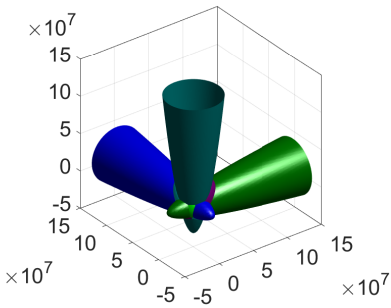

(b) Yield surfaces in stress space for closed cracks

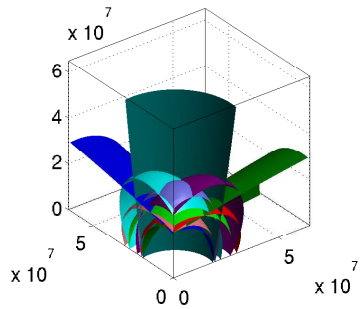

(c) Yield surfaces in compressive stress space for closed cracks

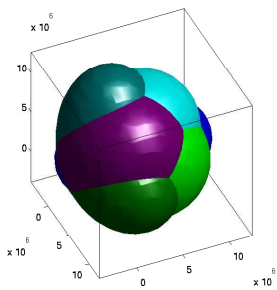

(d) Yield surfaces in stress space for open cracks

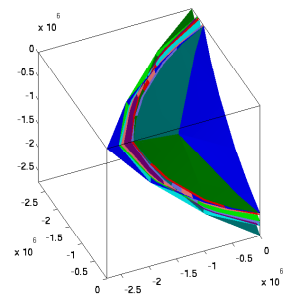

(e) Yield surfaces in tensile stress space for open cracks

Figure 3. Representation of crack yield surfaces in the 3D stress space, for a uniformly distributed damage density $\rho_i = 0.001$ in all microplane directions. Material parameters are $k_c = 278.9, \eta_c = 116.6, \alpha = 10^{-5}$ for closed crack families and $k_o = 35.9, \eta_o = 20.6, \alpha = 10^{-5}$ for open crack families. For a given state of stress, the elastic domain is the space at the intersection of all the non-smooth activated crack yield surfaces. Note the shape difference between the open crack yield surfaces and the closed crack yield surfaces, due to the expression of energy release rate Y_i.

increment of crack density of an activated crack family ($f_i > 0$) can be readily calculated by means of the consistency condition under controlled stress conditions:

$$\dot{f}_i(\rho_i, Y_i) = \frac{\partial f_i}{\partial \boldsymbol{\sigma}} : \dot{\boldsymbol{\sigma}} + \frac{\partial f_i}{\partial \rho_i}\dot{\rho}_i = 0 \tag{23}$$

The present discrete damage model requires solving all the equations that express consistency conditions for all activated crack families simultaneously. By contrast, only one consistency condition is used in Continuum Damage Mechanics models, which limits the number of crack propagation modes considered. Fig.4 shows the evolution of activated crack yield surfaces during an oedometric test (with no lateral expansion). Crack yield surfaces expand independently from each other because of the crack non interaction assumption.

Inelastic strains observed after unloading are due to residual geometric incompatibilities at the crack faces, which purely depend on the damage-driving forces Y_i. Microscopic crack yield criteria are expressed in terms of the mean stress and not only on the damage driving forces, which makes it challenging to represent the residual geometric incompatibilities that arise at crack faces after unloading. In order to overcome this limitation, we predict the evolution of inelastic strains due to these geometric incompatibilities by resorting to non-associate flow rules. We introduce discrete damage potentials, expressed as homogeneous functions of degree one in Y_i, as follows:

$$g_i(Y_i) = Y_i - C_0 \tag{24}$$

Following a non-associate flow rule, the macroscopic inelastic strain increment can be computed from the damage potential, as follows:

$$\dot{\boldsymbol{\epsilon}}^{in} = \sum_{i=1}^{M} \dot{\lambda}_i \frac{\partial g_i(Y_i)}{\partial \boldsymbol{\sigma}} = \sum_{i=1}^{M} w_i \dot{\lambda}_i (c_0 \mathbb{N}_i H(\sigma^i_{nn}) + c_1 \mathbb{T}_i) : \boldsymbol{\sigma} \tag{25}$$

Where λ_i is Lagrange multiplier for the i^{th} crack family of normal $\overrightarrow{n_i}$. Note that the non associate flow rule for the crack density is expressed as:

$$\dot{\rho}_i = \dot{\lambda}_i \frac{\partial g_i}{\partial Y_i} = \dot{\lambda}_i. \tag{26}$$

Therefore, the Lagrange multiplier is equal to the increment of crack density, because plastic deformation is coupled to damage evolution.

Numerical implementation of the multi-yield surface model

Local return mapping algorithm - closest point projection

As shown in Fig.3, the elastic domain in the proposed discrete damage model is defined by the intersection of multiple non-smooth yield surfaces. At singular points,

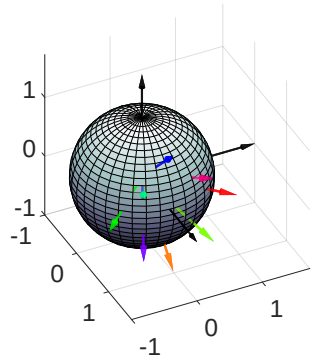

(a) Color code used for activated crack directions

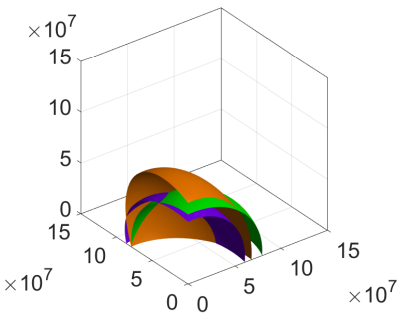

(b) Initial crack yield surfaces

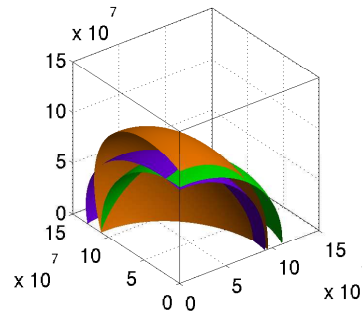

(c) Crack yield surfaces after the test

Figure 4. Evolution of activated yield surfaces ($i = 4-7, 18-20$) during an oedometer test (no lateral expansion). (b) Initial yield surfaces with a uniformly distributed crack density $\rho_i = 0.012$. (c) Activated yield surfaces at the end of the test: $\rho_{4-7} = 0.253$, $\rho_{18-21} = 0.300$. Note that some yield surfaces are superimposed due to symmetries.

the normal to this macroscopic yield surface is not unique. In order to achieve the numerical implementation of the model into a UMAT subroutine in Abaqus Finite Element program, we adopt the closest point projection algorithm presented in Simo and Hughes (1998). In the following, we note Δ a variation within a load increment and δ a variation within an iteration performed during a load increment. We use the subscript n to refer to load increment n, and the superscript (k) to refer to the iteration number.

From the constitutive relations stated in Eq. 4 and 18, we have:

$$\begin{aligned}\boldsymbol{\epsilon}^{E} &= \left[\mathbb{S}^{m} + \sum_{\alpha=1}^{M} \rho^{\alpha} w_{\alpha}(c_0 \mathbb{N}_{\alpha}^{+} + c_1 \mathbb{T}_{\alpha})\right] : \boldsymbol{\sigma} \\ \dot{\boldsymbol{\epsilon}}^{in} &= \sum_{\alpha=1}^{M} \dot{\lambda}^{\alpha} \partial_{\boldsymbol{\sigma}} g_{\alpha}(\boldsymbol{\sigma}) = \sum_{\alpha=1}^{M} \dot{\rho}^{\alpha} w_{\alpha}(c_0 \mathbb{N}_{\alpha}^{+} + c_1 \mathbb{T}_{\alpha}) : \boldsymbol{\sigma}\end{aligned} \tag{27}$$

Where $\mathbb{N}_{\alpha}^{+} = \mathbb{N}_{\alpha} H(\sigma_{nn}^{\alpha})$. In the following, we note $\mathbb{P}_{\alpha} = w_{\alpha}(c_0 \mathbb{N}_{\alpha}^{+} + c_1 \mathbb{T}_{\alpha})$ for simplicity. From the discrete Kuhn Tucker conditions, we have:

$$\text{if} \quad f_{\beta,n+1}^{trial} > 0, \quad \text{for some} \quad \alpha \in (1, 2, ..., M), \tag{28}$$

then, it is an inelastic loading step. We define the inelasitc strain residual $\boldsymbol{R}_{n+1}$ as follows:

$$-\boldsymbol{R}_{n+1} = -\Delta\boldsymbol{\epsilon}_{n+1}^{in} + \sum_{\alpha \in \mathcal{J}_{act}} \Delta\rho_{n+1}^{\alpha} \partial_{\boldsymbol{\sigma}} g_{\alpha,n+1} \tag{29}$$

Where $\mathcal{J}_{act}$ is the set of crack families that are activated. From Eq.29 the iterative correction is obtained as follows:

$$\delta\boldsymbol{\epsilon}_{n+1}^{in(k)} = \boldsymbol{R}_{n+1}^{(k)} + \sum_{\alpha \in \mathcal{J}_{act}} \Delta\rho_{n+1}^{\alpha(k)} \partial_{\boldsymbol{\sigma}\boldsymbol{\sigma}} g_{\alpha,n+1} \delta\boldsymbol{\sigma}_{n+1}^{(k)} + \sum_{\alpha \in \mathcal{J}_{act}} \delta\rho_{n+1}^{\alpha(k)} \partial_{\boldsymbol{\sigma}} g_{\alpha,n+1} \tag{30}$$

The first trial stress is given as:

$$\boldsymbol{\sigma}_{n+1}^{trial} = (\mathbb{S}^{m})^{-1} : \left[\boldsymbol{\epsilon}_{n} + \Delta\boldsymbol{\epsilon}_{n+1} - \boldsymbol{\epsilon}_{n}^{d} - \boldsymbol{\epsilon}_{n}^{in}\right] \tag{31}$$

Thereafter, iterations are performed to satisfy the yield criteria, flow rules and stress-strain relationships. Throughout the iteration process, the given total strain increment $\Delta\boldsymbol{\epsilon}_{n+1}$ is fixed. Correspondingly, the iterative change in stress is obtained as:

$$\delta\boldsymbol{\sigma}_{n+1}^{(k)} = -(\mathbb{S}^{m})^{-1} : \left[\delta\boldsymbol{\epsilon}_{n+1}^{d,(k)} + \delta\boldsymbol{\epsilon}_{n+1}^{in,(k)}\right] \tag{32}$$

Where the iterative change of damage-induced elastic strain is given by

$$\delta\boldsymbol{\epsilon}_{n+1}^{d(k)} = \sum_{\alpha=1}^{M} \rho_{n+1}^{\alpha(0)} \mathbb{P}_{\alpha} : \delta\boldsymbol{\sigma}_{n+1}^{(k)} + \boldsymbol{\sigma}_{n+1}^{(k)} : \sum_{\alpha \in \mathcal{J}_{act}} \mathbb{P}_{\alpha} \delta\rho_{n+1}^{\alpha(k)} \tag{33}$$

Making use of Eq.30 and Eq.33, Eq. 32 is rearranged as

$$\delta\boldsymbol{\sigma}_{n+1}^{(k)} = -\mathbb{C}_{c} : \left[\boldsymbol{R}_{n+1}^{(k)} + \boldsymbol{\sigma}_{n+1}^{(k)} : \sum_{\alpha \in \mathcal{J}_{act}} 2\mathbb{P}_{\alpha} \delta\rho_{n+1}^{\alpha(k)}\right] \tag{34}$$

In which the consistent stiffness matrix is defined as follows:

$$\begin{aligned}\mathbb{C}_{c} &= \left[\mathbb{S}^{m} + \sum_{\alpha=1}^{M} \rho_{n+1}^{\alpha(0)} \mathbb{P}_{\alpha} + \sum_{\alpha \in \mathcal{J}_{act}} \Delta\rho_{n+1}^{\alpha(k)} \mathbb{P}_{\alpha}\right]^{-1} \\ \partial_{\boldsymbol{\sigma}} g_{\alpha,n+1} &= \mathbb{P}_{\alpha} : \boldsymbol{\sigma}_{n+1}^{(k)}\end{aligned} \tag{35}$$

By using a first order Taylor expansion to linearize the yield criteria that apply for the sets of activated crack families, we get:

$$f^{(k)}_{\alpha,n+1} + \partial_{\boldsymbol{\sigma}} f_\alpha : \delta\boldsymbol{\sigma}^{(k)}_{n+1} + \partial_{\rho^\alpha} f_\alpha \cdot \delta\rho^{\alpha(k)}_{n+1}, \quad \alpha \in \mathcal{J}_{act} \tag{36}$$

After substituting Eq.34 into the above formulae, we obtain a system of coupled equations in which the $\delta\rho^{\alpha}_{n+1}$ are the unknowns (in blue in the following equation):

$$\begin{aligned} & f^{(k)}_{\alpha,n+1} - \partial_{\boldsymbol{\sigma}} f_\alpha : \mathbb{C}_c : \boldsymbol{R}^{(k)}_{n+1} \\ & \quad = \partial_{\boldsymbol{\sigma}} f_\alpha : \mathbb{C}_c : \sum_{\beta \in \mathcal{J}_{act}} 2\partial_{\boldsymbol{\sigma}} g_{\beta,n+1} \delta\rho^{\beta(k)}_{n+1} - \partial_{\rho^\alpha} f_\alpha \cdot \delta\rho^{\alpha(k)}_{n+1} = 0, \quad \alpha \in \mathcal{J}_{act} \end{aligned} \tag{37}$$

For the given trial stress $\boldsymbol{\sigma}^{trial}_{n+1}$, we obtain the crack density at the current increment and at the current iteration $\delta\rho^{\alpha(k)}_{n+1}$ by solving the coupled equations for all activated orientations $\alpha \in \mathcal{J}_{act}$. Then it is possible to update the correction of stress and the inelastic strain using Eqs. 34 and 30. The updated stress is then used to check the yield criteria as well as the inelastic strain residual. If $f^{(k+1)}_{\alpha,n+1}$ or $R^{(k+1)}_{n+1}$ exceeds the tolerance, the iterative process is continued until both the yield criteria and the residual fall below some given tolerances:

$$\begin{aligned} & f^{(k+1)}_{\alpha,n+1} < \text{TOL}_1, \quad \alpha \in \mathcal{J}_{act} \\ & ||\boldsymbol{R}^{(k+1)}_{n+1}|| < \text{TOL}_2 \end{aligned} \tag{38}$$

As shown in Fig.5, the set of activated crack families estimated from the trial stress may contain crack families that are actually non active. For a given increment of total strain, the true stress state must be at the intersection of the active yield surfaces only. In order to ensure the convergence from the trial stress to the true stress, the non-active crack families need to be eliminated from the set J_{act}. To do so, the sign of the iterative increment of crack density is checked after each iteration (in addition to checking the yield criteria): if the value of the crack density increment is negative, the corresponding crack family is removed from the activated crack set and the iteration is restarted by using the trial stress.

Algorithmic tangent moduli

We use the direct solver of Abaqus UMAT, in which the iterative resolution algorithm is based on Newton-Raphson method. Consequently, we need not only to update the stress and the state internal variables, but also to calculate the Jacobian matrix at the integration point level. In this section, we derive the explicit expression of the Jacobian matrix. The differentiation operator is noted as d. Note that differentiations are done at the end of iterations for each loading increment, as explained in Table 1. First, we differentiate the

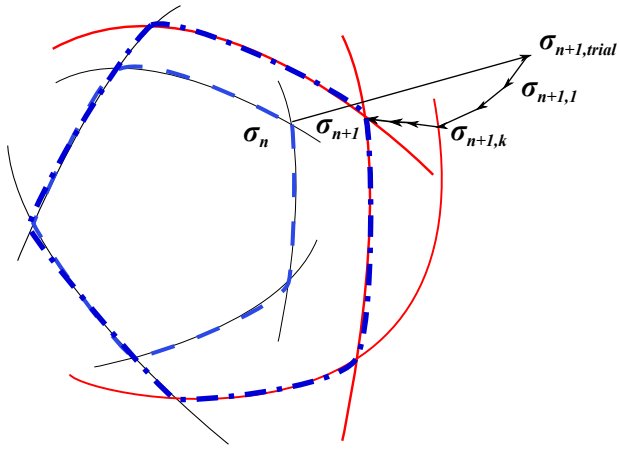

Figure 5. Geometrical representation of the return mapping algorithm used in this study: the Closest Point Projection Method is applied for multiple non-smooth yield surfaces.

stress strain relationship and the discrete flow rules, as follows:

$$\begin{aligned}
\mathrm{d}\boldsymbol{\epsilon}^{E}_{n+1} =& \left[\mathbb{S}^{m}_{n+1} + \sum_{\alpha=1}^{M} \rho^{\alpha}_{n+1}\mathbb{P}_{\alpha}\right] : \mathrm{d}\boldsymbol{\sigma}_{n+1} + \boldsymbol{\sigma}_{n+1} : \sum_{\alpha\in\mathcal{J}_{act}} \mathbb{P}_{\alpha}\mathrm{d}\rho^{\alpha}_{n+1} \\
\mathrm{d}\boldsymbol{\epsilon}^{in}_{n+1} =& \sum_{\alpha\in\mathcal{J}_{act}} \Delta\rho^{\alpha}_{n+1}\partial^{2}_{\boldsymbol{\sigma}\boldsymbol{\sigma}} g_{\alpha}(\boldsymbol{\sigma}_{n+1}) : \mathrm{d}\boldsymbol{\sigma}_{n+1} + \sum_{\alpha\in\mathcal{J}_{act}} \mathrm{d}\rho^{\alpha}_{n+1}\partial_{\boldsymbol{\sigma}} g_{\alpha}(\boldsymbol{\sigma}_{n+1}) \\
=& \sum_{\alpha\in\mathcal{J}_{act}} \Delta\rho^{\alpha}_{n+1}\mathbb{P}_{\alpha} : \mathrm{d}\boldsymbol{\sigma}_{n+1} + \sum_{\alpha\in\mathcal{J}_{act}} \mathrm{d}\rho^{\alpha}_{n+1}\mathbb{P}_{\alpha} : \boldsymbol{\sigma}_{n+1}
\end{aligned} \tag{39}$$

By substituting the above two equations into $\mathrm{d}\boldsymbol{\epsilon}_{n+1} = \mathrm{d}\boldsymbol{\epsilon}^{E}_{n+1} + \mathrm{d}\boldsymbol{\epsilon}^{in}_{n+1}$, we obtain the following relationship:

$$\begin{aligned}
&\mathrm{d}\boldsymbol{\epsilon}_{n+1} - \sum_{\alpha\in\mathcal{J}_{act}} \Delta\rho^{\alpha}_{n+1}\mathbb{P}_{\alpha} : \mathrm{d}\boldsymbol{\sigma}_{n+1} - \sum_{\alpha\in\mathcal{J}_{act}} \mathrm{d}\rho^{\alpha}_{n+1}\mathbb{P}_{\alpha} : \boldsymbol{\sigma}_{n+1} \\
=& \left[\mathbb{S}^{m}_{n+1} + \sum_{\alpha=1}^{M} \rho^{\alpha}_{n+1}\mathbb{P}_{\alpha}\right] : \mathrm{d}\boldsymbol{\sigma}_{n+1} + \boldsymbol{\sigma}_{n+1} : \sum_{\alpha\in\mathcal{J}_{act}} \mathbb{P}_{\alpha}\mathrm{d}\rho^{\alpha}_{n+1}
\end{aligned} \tag{40}$$

Equivalently,

$$\mathrm{d}\boldsymbol{\sigma}_{n+1} = \mathbb{C}_{hom} : \left[\mathrm{d}\boldsymbol{\epsilon}_{n+1} - 2\sum_{\alpha\in\mathcal{J}_{act}} \mathrm{d}\rho^{\alpha}_{n+1}\mathbb{P}_{\alpha} : \boldsymbol{\sigma}_{n+1}\right] \tag{41}$$

Where $\mathbb{C}_{hom}$ is the consistent modulus, expressed as

$$\mathbb{C}_{hom} = \left[\mathbb{S}^{m}_{n+1} + \sum_{\alpha=1}^{M} \rho^{\alpha}_{n+1}\mathbb{P}_{\alpha} + \sum_{\alpha\in\mathcal{J}_{act}} \Delta\rho^{\alpha}_{n+1}\mathbb{P}_{\alpha}\right]^{-1} \tag{42}$$

The crack density increment $\mathrm{d}\rho^{\alpha}_{n+1}$ is obtained from the discrete consistency condition by differentiating $f_\alpha(\boldsymbol{\sigma}_{n+1}) = 0$ for all activated orientations:

$$\partial_{\boldsymbol{\sigma}} f_\alpha : \mathrm{d}\boldsymbol{\sigma}_{n+1} + \partial_{\rho^\alpha} f_\alpha \cdot \mathrm{d}\rho^{\alpha}_{n+1} = 0, \quad \alpha \in \mathcal{J}_{act} \tag{43}$$

By substituting Eq.41 into Eq.43, we have

$$\begin{aligned}\partial_{\boldsymbol{\sigma}} f_\alpha(\boldsymbol{\sigma}_{n+1}) : \mathbb{C}_{hom} : \mathrm{d}\boldsymbol{\epsilon}_{n+1} =& \partial_{\boldsymbol{\sigma}} f_\alpha(\boldsymbol{\sigma}_{n+1}) : \mathbb{C}_{hom} : \Big[2 \sum_{\beta \in \mathcal{J}_{act}} \mathrm{d}\rho^{\beta}_{n+1} \mathbb{P}_\beta : \boldsymbol{\sigma}_{n+1}\Big] \\ & - \partial_{\rho^\alpha} f_\alpha(\boldsymbol{\sigma}_{n+1}) \cdot \mathrm{d}\rho^{\alpha}_{n+1}, \quad \alpha \in \mathcal{J}_{act}\end{aligned} \tag{44}$$

Equivalently,

$$\mathrm{d}\rho^{\alpha}_{n+1} = \frac{\partial_{\boldsymbol{\sigma}} f_\alpha(\boldsymbol{\sigma}_{n+1}) : \mathbb{C}_{hom} : \mathrm{d}\boldsymbol{\epsilon}_{n+1}}{2 \sum_{\beta \in \mathcal{J}_{act}} \partial_{\boldsymbol{\sigma}} f_\alpha(\boldsymbol{\sigma}_{n+1}) : \mathbb{C}_{hom} : \partial_{\boldsymbol{\sigma}} g_\beta - \partial_{\rho^\alpha} f_\alpha(\boldsymbol{\sigma}_{n+1})}, \quad \alpha \in \mathcal{J}_{act} \tag{45}$$

Note that the number of equations required to expression the relationship between $\mathrm{d}\rho^{\alpha}_{n+1}$ and $\mathrm{d}\boldsymbol{\epsilon}_{n+1}$ is equal to the number of activated yield surfaces. Substituting $\mathrm{d}\rho^{\alpha}_{n+1}$ back into Eq.41 results in a stress/strain relationship that exhibits the desired tangent moduli used in the Newton-Raphson method:

$$\frac{\mathrm{d}\boldsymbol{\sigma}_{n+1}}{\mathrm{d}\boldsymbol{\epsilon}_{n+1}} = \mathbb{C}_{hom} : \Big[\boldsymbol{I} - 2 \sum_{\alpha \in \mathcal{J}_{act}} \frac{\partial_{\boldsymbol{\sigma}} g_\alpha \otimes \partial_{\boldsymbol{\sigma}} f_\alpha : \mathbb{C}_{hom}}{2 \sum_{\beta \in \mathcal{J}_{act}} \partial_{\boldsymbol{\sigma}} f_\alpha : \mathbb{C}_{hom} : \partial_{\boldsymbol{\sigma}} g_\beta - \partial_{\rho^\alpha} f_\alpha}\Big] \tag{46}$$

The overall steps of the return mapping algorithm including the local Closest Point Projection that we implemented in ABAQUS for multiple non-smooth yield surfaces are summarized in Table 1.

Implementation verification

The implementation of the resolution algorithm is checked by comparing the model predictions obtained at the integration point (with a Matlab code) to those obtained with the Finite Element Method (one-element Abaqus model). For the tests performed at the integration point, we simulated pure shear in plane strain condition and confined compression (oedometer test) by applying strain loads of $\gamma_{12} = 2\%$ and $\epsilon_{11} = 2\%$ respectively. All the other strain components were set to zero. Pure shear tests were simulated with the FEM by applying a ± 0.0005m displacement along the edges of a square with sides of 1m in length. The oedometer test was simulated with the FEM by applying a -0.002m displacement in direction 1 and by using fixed boundaries on all the other faces of a cube. The cube edge length was 1m. 200 loading increments were used for all of the simulations. Table 2 summarizes the material parameters used for the simulations. Note that these parameters do not correspond to any specific material, although parameter values fall within the range that would be expected for a granite rock. In particular, the Young's modulus, the yield and hardening parameters represent the behavior of a rock material in tension or compression.

Table 1. Closest point projection algorithm for multiple non-smooth yield surfaces implemented in UMAT subroutines for the Abaqus direct solver.

Step	Description
1	Get the stored state variables $\rho_n^{\alpha}(\alpha = 1, ..., 42); \boldsymbol{\epsilon}_n^{in}; \boldsymbol{\sigma}_n$ from the previous increment n; Abaqus calculates the total strain increment $\Delta\boldsymbol{\epsilon}_{n+1}$
2	Initialize $\boldsymbol{\epsilon}_{n+1}^{in(0)} = \boldsymbol{\epsilon}_n^{in}; \quad \rho_{n+1}^{i(0)} = \rho_n^i$ $\boldsymbol{\sigma}_{n+1}^{trial} = \boldsymbol{\sigma}_n + \left[\mathbb{S}^m + \sum_{i=1}^{M} \rho_{n+1}^{i(0)} \mathbb{P}_i\right]^{-1} : \Delta\boldsymbol{\epsilon}_{n+1}$ Compute $f_{i,n+1}^{trial}(\boldsymbol{\sigma}_{n+1}^{trial}, \rho_{n+1}^{i(0)})$ for $i \in \{1, 2, ..., M\}, \quad \Delta\rho_{n+1}^{\alpha} = 0$
3	Check the yield criteria IF: $f_{i,n+1}^{trial} \leq 0$ for all $i \in \{1, 2, ..., M\}$ THEN: $(\cdot)_{n+1} = (\cdot)_{n+1}^{tr}$, EXIT ELSE: $\mathcal{J}_{act}^{(0)} = \{\alpha \in \{1, 2, ..., M\} \mid f_{i,n+1}^{trial} > 0\}, \quad \Delta\rho_{n+1}^{\alpha(0)} = 0$
4	Evaluate the inelastic residual $\boldsymbol{R}_{n+1}^{(k)}$ from Eq.29
5	Check the convergence of $f_{\alpha,n+1}^{(k)}(\boldsymbol{\sigma}_{n+1}^{(k)}, \rho_{n+1}^{\alpha(k-1)})$ for $\alpha \in \mathcal{J}_{act}^{(k)}$ IF: $f_{\alpha,n+1}^{(k)} <$ TOL$_1$ for all $\alpha \in \mathcal{J}_{act}^{(k)}$ and $\|\boldsymbol{R}_{n+1}^{(k)}\| <$ TOL$_2$ THEN: Provide the Jacobian matrix by using Eq.46 to ABAQUS, and EXIT
6	Compute the consistent stiffness matrix by using Eq.35. Introduce $\mathbb{C}_c$ and $\boldsymbol{R}_{n+1}^{(k)}$ in Eq.37.
7	Solve Eq.37 for $\delta\rho_{n+1}^{\alpha}, \quad \alpha \in \mathcal{J}_{act}$ Update $\Delta\rho_{n+1}^{\alpha(k+1)} = \Delta\rho_{n+1}^{\alpha(k)} + \delta\rho_{n+1}^{\alpha}$ IF: $\Delta\rho_{n+1}^{\alpha(k+1)} < 0, \quad \alpha \in \mathcal{J}_{act}^{k}$, THEN: Reset $\mathcal{J}_{act}^{(k+1)} = \{\alpha \in \mathcal{J}_{act}^{(k)} \mid \Delta\rho_{n+1}^{\alpha(k+1)} > 0\}$, Goto 4. ELSE: Calculate the inelastic strain increment correction by using Eq.30
8	Update state variables and compute the new trial stress $\boldsymbol{\epsilon}_{n+1}^{in(k+1)} = \boldsymbol{\epsilon}_n^{in} + \delta\boldsymbol{\epsilon}_{n+1}^{in(k+1)}$ $\rho_{n+1}^{\alpha(k+1)} = \rho_n^{\alpha} + \Delta\rho_{n+1}^{\alpha(k+1)}, \quad \alpha \in \mathcal{J}_{act}^{k}$ $\boldsymbol{\sigma}_{n+1}^{(k+1)} = \left[\mathbb{S}^m + \sum_{\alpha=1}^{M} \rho_{n+1}^{\alpha(k+1)} \mathbb{P}_{\alpha}\right]^{-1} : (\boldsymbol{\epsilon}_n + \mathrm{d}\boldsymbol{\epsilon}_{n+1} - \boldsymbol{\epsilon}_{n+1}^{in(k+1)})$ Goto 5.

Table 2. Material parameters used for the verification of the implementation of the algorithm

Elasticity		Initial State		Damage function				
E_0	ν_0	a_0	$\mathcal{N}$	α	k_c	η_c	k_o	η_o
GPa	$-$	L	N/L^3	$-$	Pa	Pa	Pa	Pa
53.5	0.35	0.05	960	10^{-5}	278.9	116.6	35.9	20.6

Fig.6 shows the results. For all the cases simulated, both the linear elastic response and the non-linear damaged response are well captured by the discrete damage model. The difference between the stress/strain curves obtained at the material point (Matlab) and in the one-element FEM model (Abaqus) is negligible. Note that the reason why the stress/strain curve is almost linear in the oedometer test is because the lateral pressure increases the hardening effects. Fig.6(b) shows the crack density distribution for the oedometer test. Results show that only mode II crack propagation driven by deviatoric stress is possible. As a result, the direction normal to the activated crack planes is closer to the loading direction than the direction normal to the inactivated crack planes . Fig.6(d) shows the crack density distribution for the pure shear test. During a pure shear path, principal tension and compression components rotate by 45 degree with respect to the shear axes 1 and 2. The resistance to tension for brittle material is much less than the shear resistance, which explains the predominance of crack propagation in planes of normal oriented by an angle of 45 degrees to the horizontal or vertical. Note that because the Matlab simulations are done in plane strain and the Abaqus simulations are done in 3D, there is a small discrepancy between the two stress/strain curves at the later stage of the pure shear test (Fig.6(c)). We conclude that the proposed discrete damage model is suitable to track anisotropic crack density evolution and that the Closest Point Projection algorithm implemented in UMAT is accurate.

Damage model Calibration and Numerical Applications

Principle of the calibration algorithm

The proposed discrete damage model depends on 9 constitutive parameters, which can be grouped into 3 categories: elasticity, initial state, and damage (Table 2). The model can account for intrinsic anisotropy (i.e. with anisotropy not induced by micro-crack propagation), if different values are chosen for the reference (initial) microcrack radius (a_0) and the initial number of microcracks $\mathcal{N} = \frac{N}{\Omega_r}$ for different crack orientations. By construction of the yield criteria, two independent loading paths are needed in tension and in compression to calibrate the material parameters (depending whether the unilateral condition is satisfied or not). If the simulation only involves compressive stress (respectively tensile stress), the two damage function parameters k_o, η_o (respectively k_c, η_c) can be omitted.

We used the Interior Point Algorithm programmed in Matlab to determine the unknown vector $\boldsymbol{B} = (E_0, \nu_0, a_0, \mathcal{N}, \alpha, k_c, \eta_c, k_o, \eta_o)$ that minimizes the squared residual of the distance between experimental results y_i and numerical predictions $f(\boldsymbol{x}, \boldsymbol{B})$. The residual that is minimized iteratively is defined as:

$$R(\boldsymbol{B}) = \sum_{i=1}^{n} [y_i - f(\boldsymbol{x}, \boldsymbol{B})]^2 \tag{47}$$

Where $\boldsymbol{x}$ stands for the vector of known input variables (e.g., strain or stress, depending whether the load is controlled in force or displacement). The algorithm is initialized with an initial guess and a reasonable range of values for the coefficients of the unknown

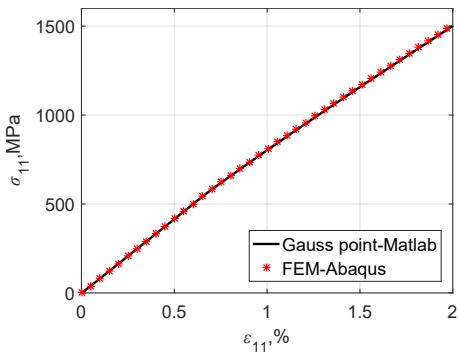

(a) Stress/strain curves - Oedometer Test

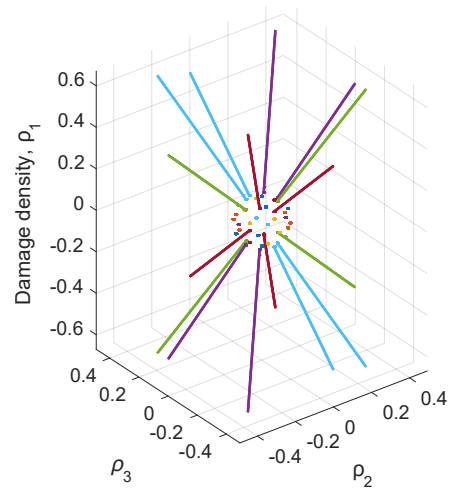

(b) Crack density Distribution - Oedometer Test

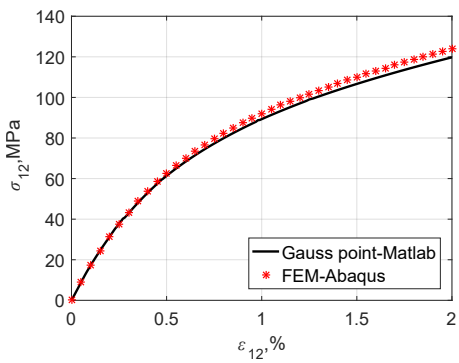

(c) Stress/strain curves - Pure Shear Test

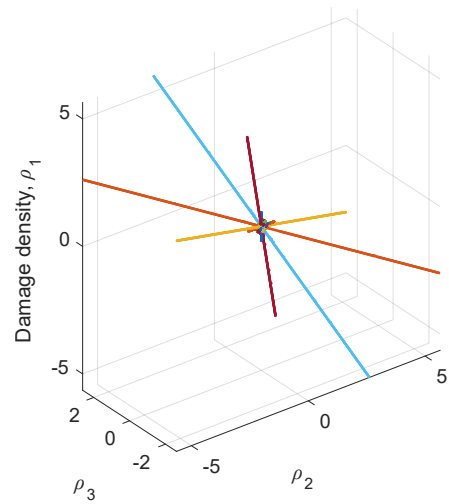

(d) Crack density Distribution - Pure Shear Test

Figure 6. Verification and accuracy tests. Comparison of the stress/strain curves obtained at the material point and with the FEM for an oedometer test (a) and for a pure shear test (c). The corresponding distributions of damage density are shown in Figures (b) and (d) respectively.

parameter vector $\boldsymbol{B}$. Then, the tests with the discrete damage model are simulated at the material point, and the value of the residual $R(\boldsymbol{B})$ is updated iteratively. The gradient of the residual $R(\boldsymbol{B})$ with respect to each parameter listed in the vector $\boldsymbol{B}$ is calculated.

Table 3. Model parameters calibrated against triaxial compression tests reported in Papanikolaou and Kappos (2007) for high strength concrete

Elasticity		Initial State		Damage function		
E_0	ν_0	a_0	$\mathcal{N}$	α	k_c	η_c
GPa	$-$	L	N/L^3	$-$	Pa	Pa
53.6	0.22	2×10^{-4}	8178	3.3×10^{-5}	34.3	615.7

This gradient of residual is used to minimize the difference between numerical and experimental stress-strain curves, as follows:

$$\boldsymbol{B}_{n+1} = \boldsymbol{B}_n - \gamma_n \Delta R(\boldsymbol{B}) \tag{48}$$

Where γ_n is the barrier parameter, which is updated at each iteration step in the Interior Point Algorithm. The procedure is described in detail in (Byrd et al. 2000; Waltz et al. 2006).

Triaxial compression test for concrete

We first calibrate and validate the discrete damage model against a series of triaxial compression tests performed on high strength concrete by Papanikolaou and Kappos (2007). The experimental stress/strain curves obtained with confinements of 4 & 12 MPa were used for calibration. Experimental data obtained with a confining pressure of 8 MPa was used for validation. The soil mechanics sign convention was adopted throughout the paper (with compression counted positive). Note that only the portion of the experimental data obtained before the peak of the stress/strain peak was used, because the proposed discrete damage model is only valid for non-interacting cracks. Table 3 summarizes the values of the calibrated material parameters.

Fig.7(a) shows the results obtained after model calibration for confining pressures of $\sigma_3 = 4, 8\&12$ MPa. The excellent match between numerical and experimental curves, especially for the test performed at 8 MPa (used for model validation) show that the discrete damage model allows representing the non-linear behavior of concrete subject to compressive damage. Because the yield criteria depend on the mean stress via the term $\alpha \mathrm{Tr}\boldsymbol{\sigma}$, the model can capture the increase of the yield stress σ_y with increasing confining pressure σ_3, as can be seen from the evolution of the crack densities in the different directions of space in Fig.7(b). The discrete damage model highlights the difference of crack density magnitude among the activated crack families. Overall, the performance of the discrete damage model for the calibrated parameters is very satisfactory for closed micro-crack propagation.

With the parameters calibrated above for concrete, we simulated a triaxial compression test performed under a confinement 4 MPa with the Finite Element Method (FEM). Following the standards of the American Society for Testing and Materials (ASTM), we modeled a cylindrical concrete sample of diameter 0.1 m and length 0.2 m. Due to symmetries, only $1/8$ of sample is meshed in Abaqus, as shown in Fig.8. In total,

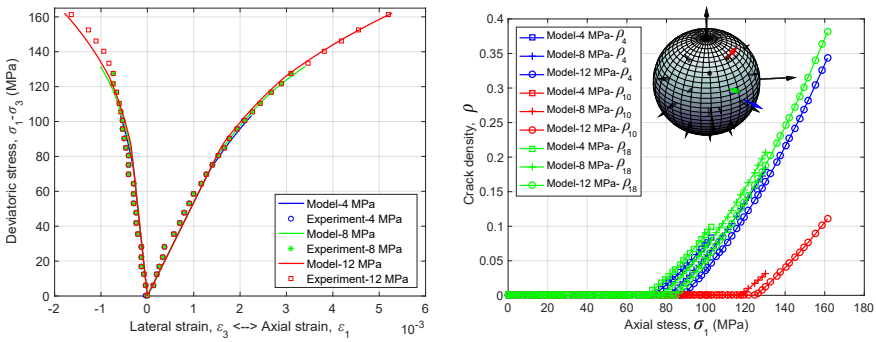

(a) Triaxial test stress-strain curves (b) Evolution of crack densities during triaxial tests

Figure 7. Calibration and validation of the discrete damage model parameters against experimental stress-strain curves obtained during triaxial compression tests performed on concrete under various confining pressures. (a) Results of tests performed with a confining pressure of $\sigma_3 = 4\&12$ MPa were used to calibrate the model. Experimental results obtained for a confining pressure of $\sigma_3 = 8$ MPa were employed to validate the calibration. (b) Evolution of the typical damage densities in different directions with the calibrated parameters, for the three confining pressures.

4,000 hexahedral elements were used. Besides the symmetry boundary conditions, a zero horizontal displacement (in directions x_1 and x_2) was imposed at the top surface (perpendicular to x_3 axis), in order to mimic the friction effect between the steel plate and the concrete sample. After applying a 4 MPa hydrostatic confinement on all the external boundaries, the top surface was subjected to a vertical displacement of 0.0003 m. Fig.8 shows the crack density distribution for all activated crack families at the end of the test. By contrast with the oedometer test, the confining pressure is maintained to a constant value, therefore, more crack families are activated during the triaxial compression test. As expected, the space variations of crack density differs from one crack plane orientation to the other. Note however that for all activated crack families, the highest crack density is reached at the edge of the sample that is in contact with the steel plate. This phenomenon is a frictional boundary effect, which explains macro fracture initiation in isotropic and homogeneous samples. It can also be noted that for all damage directions, activated cracks concentrate in the center of the sample. This result is in agreement with experimental measures of damage based on acoustic emission velocity and lateral deformation. Given that cracks of different directions are superposed, it is clear that the inner part of the sample is the most damaged during the test. The proposed discrete damage model provides a detailed description of the fabric of materials damaged in compression with only 3 damage parameters (α, k_c, η_c), 2 initial crack parameters (a_0 and $\mathcal{N}$) and 2 elasticity parameters (E_0 and ν_0). This is a significant gain of information compared to former damage models implemented in FEM, which are formulated with second-order damage tensor at most (Xu and Arson 2015; Jin et al. 2016).

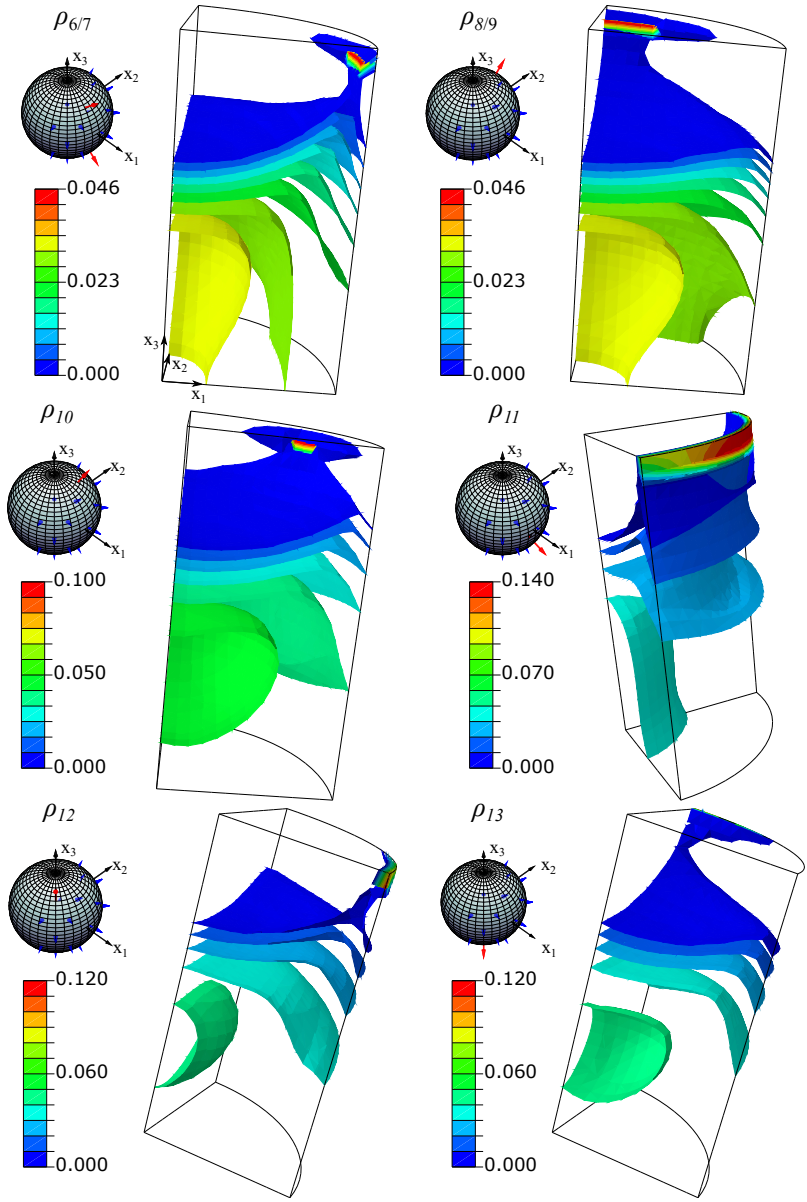

Figure 8. FEM simulation of a triaxial compression test performed on an ASTM concrete sample subjected to a 4 MPa confining pressure. Isosurfaces of the crack densities for the activated crack families.

Table 4. Model parameters calibrated against uniaxial tension tests reported in Bazant and Pijaudier-Cabot (1989) for concrete.

Elasticity		Initial State		Damage function		
E_0	ν_0	a_0	$\mathcal{N}$	α	k_o	η_o
GPa	$-$	L	N/L^3	$-$	Pa	Pa
27.0	0.23	4.8×10^{-3}	485	0.5×10^{-5}	95.0	0.095

Hassanzadeh's direct tension test for concrete

In most brittle materials, uniaxial tension results in a highly localized macroscopic crack propagation followed by tensile failure. The stress-strain curve recorded during uniaxial tension tests cannot truly reflect the material behavior because the strain is not uniform throughout the sample. That is the reason why Bazant and Pijaudier-Cabot (1989) designed a specific testing apparatus, in which the concrete sample is glued to parallel thin-steel rods. The testing procedure allows obtaining the stress strain curve even when micro-cracks are diffused throughout the sample. We used the hardening portion of the stress/strain curves reported in Bazant and Pijaudier-Cabot (1989) in order to calibrate the discrete damage model for open crack propagation modes (i.e., when the unilateral condition is satisfied). Calibration results are given in Table 4 and shown in Fig.9(a), in which the soil mechanics sign convention was adopted (compression counted positive). Concrete behaves as a perfectly plastic material prior to yielding. The hardening behavior is captured, but as explained before, the post-peak behavior cannot be represented with the dilute homogenization scheme adopted here. Note that because all the cracks are initially closed, the cracks that propagate during the test are those in the planes perpendicular to the loading direction, as can be seen from the evolution of ρ_1 in Fig.9(b).

In order to demonstrate the capability of the proposed model to predict the behavior of brittle solids in tension, we simulated Hassanzadeh's direct tension test Hassanzadeh (1992). A four-edge notched specimen was assigned the calibrated parameters listed in Table 4. The specimen geometry and the applied boundary conditions are shown in Fig.10. Due to symmetries, only $1/8$ of sample was modeled. A vertical displacement field was imposed at the bottom face of the domain ($u = 0.01$ mm). We used a coarse mesh with 9,943 3D hexahedral elements and a fine mesh with 35,550 elements.

The isosurfaces of horizontal crack density (i.e. density of crack planes perpendicular to the tensile loading axis) are shown in Fig.11 for both the coarse and fine meshes. Of course, in this purely hypothetical simulation test the high magnitude reached by ρ_3 is not realistic: physically, a macroscopic horizontal fracture would propagate during the test, which cannot be captured by using a dilute scheme homogenization scheme. Interestingly, results show that micro-cracks propagate from the edges to the center of the central part of the sample, which is in agreement with experimental observations. Note that the maximum crack density calculated with the coarse mesh is less than with the fine mesh, and the extent of the damaged zone is larger with the coarse mesh than with

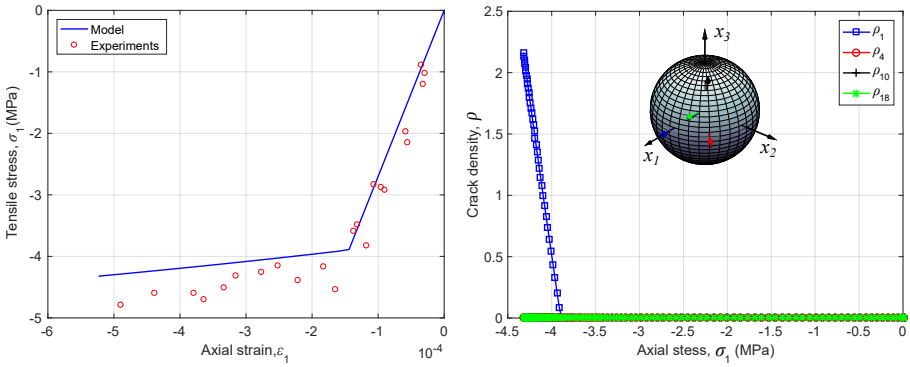

(a) Stress - strain curves - Uniaxial Tension Test (b) Crack density evolution - Uniaxial Tension Test

Figure 9. Calibration of the discrete damage model against uniaxial tension experimental data Bazant and Pijaudier-Cabot (1989) for open crack propagation.

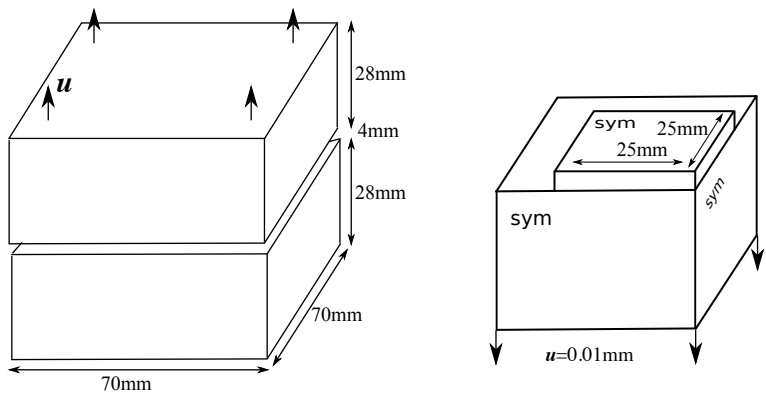

Figure 10. Hassanzadeh's direct tension test: problem definition, simulation domain and boundary conditions.

the fine mesh. To avoid this problem of mesh-dependency, a non-local discrete damage model formulation is required. Such a regularization work goes beyond the scope of the present study, but is currently undertaken by the authors. For both mesh refinements, the extent of the damaged zone exceeded the size of a single Finite Element. In addition to the crack families perpendicular to the loading direction (x_3-axis), four crack sets were activated during the test, as shown in Fig.12. As expected, these four directions are the closest to the loading direction. Overall, the discrete damage model can predict micro crack propagation in tension at a very low yield stress. The authors work on combining the model implemented in FEM with Cohesive Zone Elements Jin et al. (2016); Jin and Arson (2016) or XFEM Comi et al. (2007), which will allow simulating the evolution of the damage process zone evolution around macroscopic fractures.

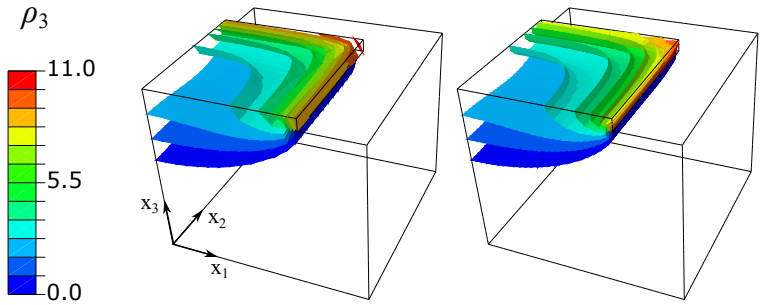

Figure 11. Hassanzadeh's direct tension test: Final horizontal crack density isosurfaces for the coarse (left) and fine (fine) meshes.

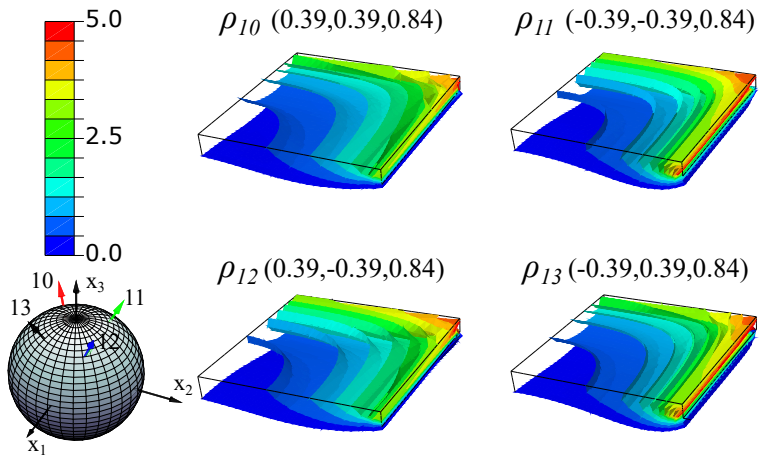

Figure 12. Hassanzadeh's direct tension test: Isosurfaces of damage density for non-horizontal activated crack families obtained from fine mesh results.

Plane stress tension test for a fiber-reinforced composite

In the following, we study the activation and propagation of crack sets in a fiber-reinforced composite subjected to a plane stress tensile test. The fibers are assumed to have a much higher tensile strength than the matrix, and are modeled as linear elastic materials. The matrix material is assigned the discrete damage model, in which only open crack propagation modes are considered. The material parameters adopted in the simulations are listed in Table 5. Note that the matrix material's Young's modulus is less than that of the fibers. We compare the results obtained when fibers are either aligned or perpendicular to the direction of the applied tension to those obtained when the fibers are all oriented by an angle of 45^o to the tensile direction, as shown in Fig.13. Simulations were done in 3D. The elements' thickness was 0.1 m. The same boundary conditions were adopted in both cases. Hexahedral elements with an average edge size of 0.025

Table 5. Model parameters used in the simulation of tension tests on a fiber-reinforced composite.

Elasticity (fibers)		Elasticity (matrix)		Initial State		Damage function		
E_0	ν_0	E	ν	a_0	$\mathcal{N}$	α	k_o	η_o
GPa	$-$	GPa	$-$	L	N/L^3	$-$	Pa	Pa
50	0.3	35	0.25	0.001	120	2×10^{-5}	20	24

m were used in both cases. The mesh was structured for the simulation of tension in the axis of the fibers, and random for the simulation of tension at 45^o from the axis of the fibers (due to the complexity of the geometry). At the interface between the fibers and the matrix, nodes were shared, i.e. the two materials were perfectly bonded so that the interface friction was not considered. The composite plates were assumed to be symmetric about the horizontal and vertical axes, therefore fixed displacements were applied at the bottom and left boundaries of the domain. A displacement of 0.01 mm was applied normal to the top boundary. On the right boundary, a zero horizontal displacement and a zero vertical stress were imposed.

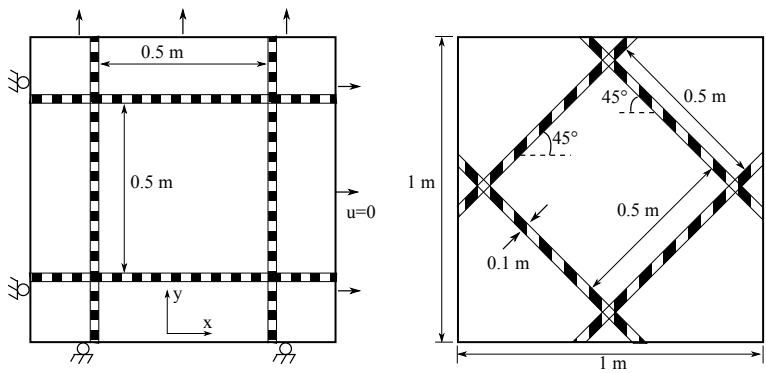

Figure 13. Problem definition and boundary conditions for the simulation of tension tests on a fiber-reinforced composite.

Fig.14 shows the distributions of horizontal and vertical stress for both composites. Note that results are displayed in a plane located at at mid-thickness of the plates in the x_3 direction (thickness direction). As expected, fibers bear most of the load applied due to their higher stiffness. Note that when fibers are aligned with a principal stress direction, all the stress in that direction concentrates in the fibers. For example, the vertical stress (in x_2 direction) is concentrated along the vertical fibers, and the horizontal stress (in x_1 direction) is concentrated along the horizontal fibers. When tension is applied at an angle of 45^o to the fibers, the maximum vertical stress reached in the fibers is less than in vertical fibers, and the maximum horizontal stress reached in the fibers is more than in horizontal fibers.

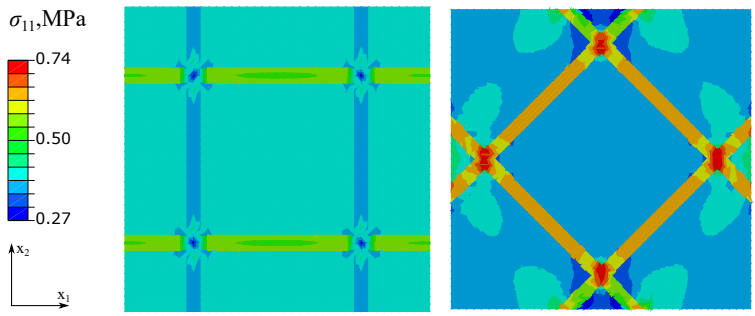

(a) Horizontal stress distribution

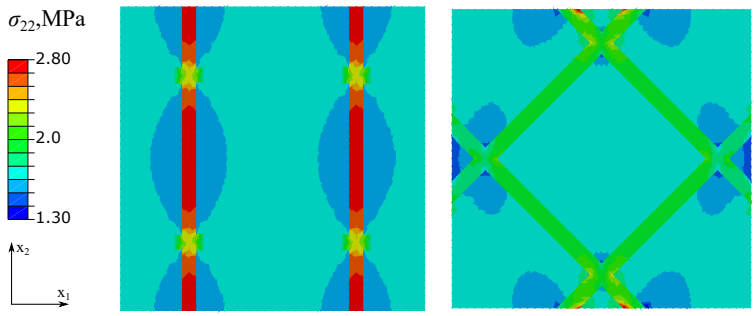

(b) Vertical stress distribution

Figure 14. Distribution of horizontal and vertical stress in composites with various orientations of fiber reinforcements.

The effect of fiber orientation on the distribution of cracks in the matrix material is illustrated in Fig.15. Note the color code used to represent the families of activated crack planes: ρ_1, ρ_2 in green, ρ_4 in blue and ρ_{14} in red. The variations of ρ_4 (respectively ρ_{14}) inside the domain are similar to those of $\rho_{5,25,26}$ (respectivley $\rho_{15-17,36-39}$), due to the symmetry in crack orientations. ANote that all the crack families that are activated during the test are inside the plane of x_1, x_2, or have a very small component in axis x_3. The smallest and largest of all possible values reached by the crack densities are obtained at the intersection of the inclined fiber reinforcements. Cracks also concentrate at the boundary, close to the inclined fibers. Crack densities are more uniformly distributed in the composites with non-inclined fibers. This example illustrates the benefits of accounting for fiber orientation in the design of thin structures subjected to tension, such as the walls of pressurized vessels. In this particular case, putting fibers in the axis of the tensile load will allow reducing the load borne by the matrix material, and therefore, to reduce the density of tensile cracks. Fiber intersections are the parts of the composite plate that are the most exposed to tensile damage, and need to be checked in priority for monitoring purposes. The proposed discrete damage model thus provides

useful predictions of crack patterns in brittle materials subject to mixed mode crack propagation, with a small number of material parameters which all have a sound physical meaning.

Conclusions

The discrete damage model presented in this paper is based on a dilute homogenization scheme, which allows summing up the energy potentials stored in the displacement jumps of crack families of different orientations to represent the energy stored at the scale of the Representative Volume Element(RVE). 42 microplane orientations are considered. Closed cracks propagate in pure mode II, whereas open cracks propagate in mixed mode (I/II). The elastic domain is at the intersection of the yield surfaces of the activated crack families. These surfaces are not smooth. In order to solve for the 42 crack densities, a Closest Point Projection algorithm is adopted locally. The irreversible strains at the RVE scale are obtained by using a Newton-Raphson algorithm. To the authors' best knowledge, this is the first time that a discrete damage model accounting for two crack propagation modes is successfully implemented in a Finite Element program. The proposed damage model was rigorously calibrated for both compressive and tensile stress paths. Simulations of triaxial compression tests showed that the transition between brittle and ductile behavior at increasing confining pressure can be captured. The cracks' density, orientation and location predicted in the simulations are in agreement with experimental observations made during compression and tension tests, and accurately show the difference between tensile and compressive strength. Plane stress tension tests simulated for a fiber-reinforced brittle material also demonstrated that the model can be used to interpret crack patterns, design composite structures and recommend reparation techniques for structural elements subjected to multiple damage mechanisms. This is a significant asset compared to the capabilities of former Continuum Damage Mechanics models used in FEMs. More work is needed to regularize the model, avoid mesh dependence and extend the formulation to interacting sets of micro-cracks.

Acknowledgements

Funding for this research work was provided by the U.S. National Science Foundation (NSF), grants 1449501 (Engineering Research Center on Bio-mediated and Bio-inspired Geotechnics) and 1552368 (CAREER: Multiphysics Damage and Healing of Rocks for Performance Enhancement of Geo-Storage Systems - A Bottom-Up Research and Education Approach).

References

Amitrano D, Grasso JR and Hantz D (1999) From diffuse to localised damage through elastic interaction. Geophysical Research Letters 26(14): 2109–2112.

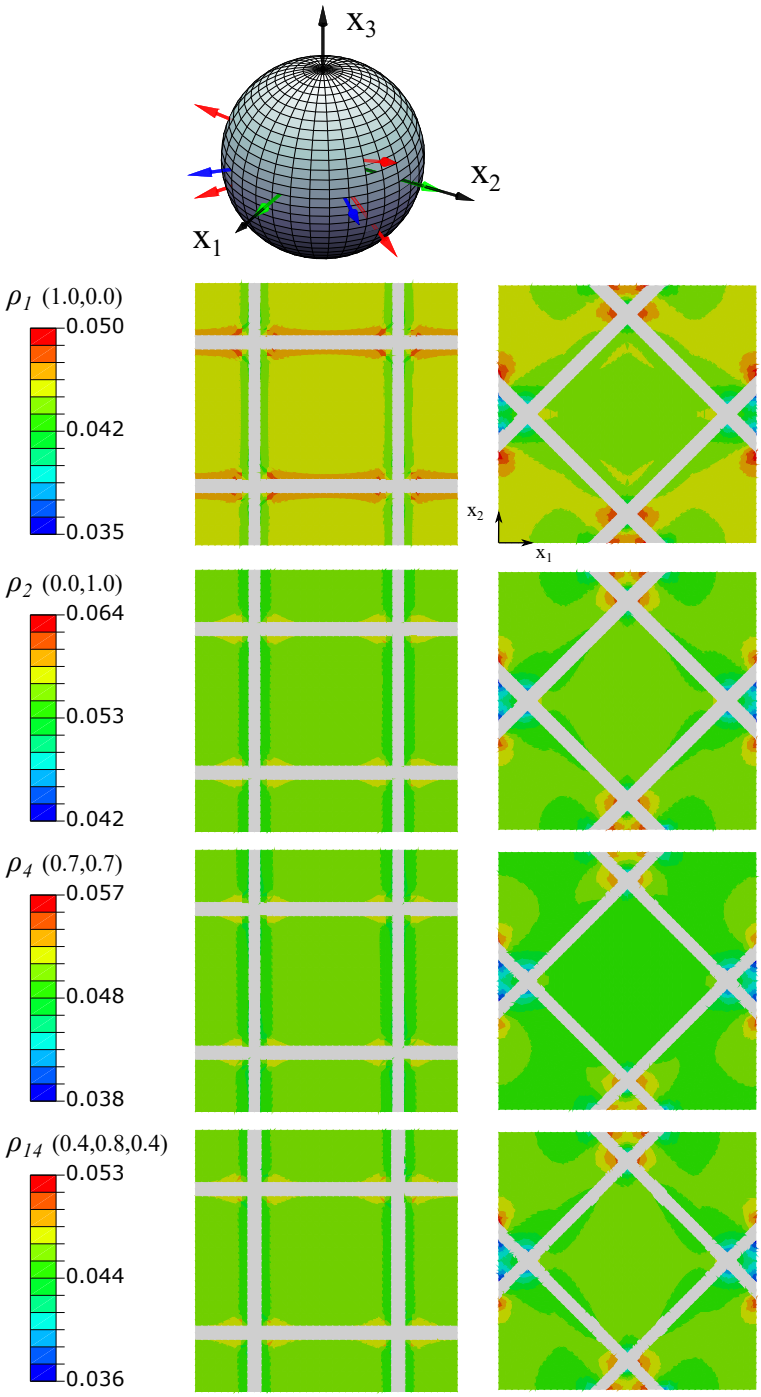

Figure 15. Crack density distribution for typical directions inside the base material.

Bažant P and Oh B (1986) Efficient numerical integration on the surface of a sphere. ZAMM-Journal of Applied Mathematics and Mechanics/Zeitschrift für Angewandte Mathematik und Mechanik 66(1): 37–49.

Bazant ZP and Pijaudier-Cabot G (1989) Measurement of characteristic length of nonlocal continuum. Journal of Engineering Mechanics 115(4): 755–767.

Blair S and Cook N (1998) Analysis of compressive fracture in rock using statistical techniques: Part i. a non-linear rule-based model. International Journal of Rock Mechanics and Mining Sciences 35(7): 837–848.

Budiansky B and O'connell RJ (1976) Elastic moduli of a cracked solid. International Journal of Solids and Structures 12(2): 81–97.

Byrd RH, Gilbert JC and Nocedal J (2000) A trust region method based on interior point techniques for nonlinear programming. Mathematical Programming 89(1): 149–185.

Chaboche JL (1981) Continuous damage mechanics—a tool to describe phenomena before crack initiation. Nuclear Engineering and Design 64(2): 233–247.

Chaboche JL (1988) Continuum damage mechanics: Part ii—damage growth, crack initiation, and crack growth. Journal of applied mechanics 55(1): 65–72.

Chaboche JL (1992) Damage induced anisotropy: on the difficulties associated with the active/passive unilateral condition. International Journal of Damage Mechanics 1(2): 148–171.

Chaboche JL (1993) Development of continuum damage mechanics for elastic solids sustaining anisotropic and unilateral damage. International Journal of Damage Mechanics 2(4): 311–329.

Chiarelli AS, Shao JF and Hoteit N (2003) Modeling of elastoplastic damage behavior of a claystone. International Journal of Plasticity 19(1): 23–45.

Clayton J (2010) Deformation, fracture, and fragmentation in brittle geologic solids. International Journal of Fracture 163(1-2): 151–172.

Collins I and Houlsby G (1997) Application of thermomechanical principles to the modelling of geotechnical materials. In: Proceedings of the Royal Society of London A: Mathematical, Physical and Engineering Sciences, volume 453. The Royal Society, pp. 1975–2001.

Comi C, Mariani S and Perego U (2007) An extended fe strategy for transition from continuum damage to mode i cohesive crack propagation. International Journal for Numerical and Analytical Methods in Geomechanics 31(2): 213.

Comi C and Perego U (2001) Fracture energy based bi-dissipative damage model for concrete. International Journal of Solids and Structures 38(36): 6427–6454.

Ehret A, Itskov M and Schmid H (2010) Numerical integration on the sphere and its effect on the material symmetry of constitutive equations—a comparative study. International journal for numerical methods in engineering 81(2): 189–206.

Espinosa H (1995) On the dynamic shear resistance of ceramic composites and its dependence on applied multiaxial deformation. International journal of solids and structures 32(21): 3105–3128.

Fang Z and Harrison J (2002) Development of a local degradation approach to the modelling of brittle fracture in heterogeneous rocks. International Journal of Rock Mechanics and Mining

Sciences 39(4): 443–457.

Feng XQ and Yu SW (2010) Damage micromechanics for constitutive relations and failure of microcracked quasi-brittle materials. International Journal of Damage Mechanics 19(8): 911–948.

Frémond M and Nedjar B (1996) Damage, gradient of damage and principle of virtual power. International Journal of Solids and Structures 33(8): 1083–1103.

Gambarotta L and Lagomarsino S (1993) A microcrack damage model for brittle materials. International Journal of Solids and Structures 30(2): 177–198.

Halm D and Dragon A (1996) A model of anisotropic damage by mesocrack growth; unilateral effect. International Journal of Damage Mechanics 5(4): 384–402.

Hassanzadeh M (1992) Behaviour of fracture process zones in concrete influenced by simultaneously applied normal and shear displacements. PhD Thesis, Lund University.

Horii H and Nemat-Nasser S (1983) Overall moduli of solids with microcracks: load-induced anisotropy. Journal of the Mechanics and Physics of Solids 31(2): 155–171.

Horii H and Nemat-Nasser S (1986) Brittle failure in compression: splitting, faulting and brittle-ductile transition. Philosophical Transactions of the Royal Society of London A: Mathematical, Physical and Engineering Sciences 319(1549): 337–374.

Jin W and Arson C (2016) Simulation of mode ii unconstrained fracture path formation coupled with continuum anisotropic damage propagation in shale. Georgia Institute of Technology.

Jin W, Xu H, Arson C and Busetti S (2016) Computational model coupling mode ii discrete fracture propagation with continuum damage zone evolution. International Journal for Numerical and Analytical Methods in Geomechanics .

Jing L (2003) A review of techniques, advances and outstanding issues in numerical modelling for rock mechanics and rock engineering. International Journal of Rock Mechanics and Mining Sciences 40(3): 283–353.

Ju J (1989) On energy-based coupled elastoplastic damage theories: constitutive modeling and computational aspects. International Journal of Solids and structures 25(7): 803–833.

Ju J (1991) On two-dimensinal self-consistent micromechanical damage models for brittle solids. International Journal of Solids and Structures 27(2): 227–258.

Ju J and Lee X (1991) Micromechanical damage models for brittle solids. part i: tensile loadings. Journal of Engineering Mechanics 117(7): 1495–1514.

Kachanov M (1992) Effective elastic properties of cracked solids: critical review of some basic concepts. Applied Mechanics Reviews 45(8): 304–335.

Kachanov ML (1982a) A microcrack model of rock inelasticity part i: Frictional sliding on microcracks. Mechanics of Materials 1(1): 19–27.

Kachanov ML (1982b) A microcrack model of rock inelasticity part ii: propagation of microcracks. Mechanics of Materials 1(1): 29–41.

Kachanov ML, Shafiro B and Tsukrov I (2013) Handbook of elasticity solutions. Springer Science & Business Media.

Krajcinovic D (1989) Damage mechanics. Mechanics of materials 8(2): 117–197.

Krajcinovic D, Basista M and Sumarac D (1991) Micromechanically inspired phenomenological damage model. Journal of Applied Mechanics 58(2): 305–310.

Krajcinovic D and Fanella D (1986) A micromechanical damage model for concrete. Engineering Fracture Mechanics 25(5): 585–596.

Krajcinovic D and Sumarac D (1989) A mesomechanical model for brittle deformation processes: Part i. Journal of Applied Mechanics 56(1): 51–56.

Lee X and Ju J (1991) Micromechanical damage models for brittle solids. part ii: compressive loadings. Journal of Engineering Mechanics 117(7): 1515–1536.

Lehner F and Kachanov M (1996) On modelling of 'winged" cracks forming under compression. International Journal of Fracture 77(4): R69–R75.

Levasseur S, Collin F, Charlier R and Kondo D (2013) On micromechanical damage modeling in geomechanics: Influence of numerical integration scheme. Journal of Computational and Applied Mathematics 246: 215–224.

Lubarda V, Krajcinovic D and Mastilovic S (1994) Damage model for brittle elastic solids with unequal tensile and compressive strengths. Engineering Fracture Mechanics 49(5): 681–697.

Mazars J and Pijaudier-Cabot G (1989) Continuum damage theory-application to concrete. Journal of Engineering Mechanics 115(2): 345–365.

Mori T and Tanaka K (1973) Average stress in matrix and average elastic energy of materials with misfitting inclusions. Acta metallurgica 21(5): 571–574.

Murakami S (1988) Mechanical modeling of material damage. Journal of Applied Mechanics 55(2): 280–286.

Papanikolaou VK and Kappos AJ (2007) Confinement-sensitive plasticity constitutive model for concrete in triaxial compression. International Journal of Solids and Structures 44(21): 7021–7048.

Pensee V and Kondo D (2003) Micromechanics of anisotropic brittle damage: comparative analysis between a stress based and a strain based formulation. Mechanics of materials 35(8): 747–761.

Pensée V, Kondo D and Dormieux L (2002) Micromechanical analysis of anisotropic damage in brittle materials. Journal of Engineering Mechanics 128(8): 889–897.

Potyondy D and Cundall P (2004) A bonded-particle model for rock. International journal of rock mechanics and mining sciences 41(8): 1329–1364.

Simo J and Hughes TJ (1998) Computational inelasticity, volume 7 of interdisciplinary applied mathematics.

Simo J and Ju J (1987) Strain-and stress-based continuum damage models—i. formulation. International journal of solids and structures 23(7): 821–840.

Swoboda G and Yang Q (1999a) An energy-based damage model of geomaterials—i. formulation and numerical results. International journal of solids and structures 36(12): 1719–1734.

Swoboda G and Yang Q (1999b) An energy-based damage model of geomaterials—ii. deductionof damage evolution laws. International journal of solids and structures 36(12): 1735–1755.

Tang C, Liu H, Lee P, Tsui Y and Tham L (2000) Numerical studies of the influence of microstructure on rock failure in uniaxial compression—part i: effect of heterogeneity. International Journal of Rock Mechanics and Mining Sciences 37(4): 555–569.

Waltz RA, Morales JL, Nocedal J and Orban D (2006) An interior algorithm for nonlinear optimization that combines line search and trust region steps. Mathematical Programming 107(3): 391–408.

Weibull W (1951) Wide applicability. Journal of applied mechanics 103: 293–297.

Xu H and Arson C (2015) Mechanistic analysis of rock damage anisotropy and rotation around circular cavities. Rock Mechanics and Rock Engineering : 1–17.

Yu SW and Feng XQ (1995) A micromechanics-based damage model for microcrack-weakened brittle solids. Mechanics of Materials 20(1): 59–76.

Yuan S and Harrison J (2006) A review of the state of the art in modelling progressive mechanical breakdown and associated fluid flow in intact heterogeneous rocks. International Journal of Rock Mechanics and Mining Sciences 43(7): 1001–1022.

Zhu Q, Kondo D and Shao J (2008) Micromechanical analysis of coupling between anisotropic damage and friction in quasi brittle materials: role of the homogenization scheme. International Journal of Solids and Structures 45(5): 1385–1405.

Zhu Q, Kondo D and Shao JF (2009) Homogenization-based analysis of anisotropic damage in brittle materials with unilateral effect and interactions between microcracks. International Journal for Numerical and Analytical Methods in Geomechanics 33(6): 749–772.